Impedance Space Method: Time-Independent Parametric Ellipses for Robot Compliant Control

Leonardo F. Dos Santos, Cícero Zanette, Elisa G. Vergamini, Lucca Maitan, and Thiago Boaventura

***Abstract*—This paper proposes a novel 3D graphical representation for impedance control, called the *impedance space*, to foster the analysis of the dynamic behavior of robotic compliant controllers. The method overcomes limitations of existing 2D graphical approaches by incorporating mass, stiffness, and damping dynamics, and associates the impedance control parameters with linear transformations to plot a parametric 3D ellipse and its projections in 2D for a mass-spring-damper impedance under sinusoidal reference. Experimental evaluation demonstrates the effectiveness of the proposed representation for analysis of impedance control. The method applies to various compliant control topologies and can be extended to other model-based control approaches.**

Link to graphical and video abstracts, and to code: https://latamt.ieeer9.org/index.php/transactions/article/view/9874

***Index Terms*—Impedance control, Force control, Human-robot interaction**

I. Introduction

ROBOTIC compliant actuation is crucial for safe physical interactions with unknown environments, including humans and assets. Since the 1970s, studies on muscle activation and the central nervous system have introduced mechanical impedance as a key concept, as cited in [1]. Drawing from these biological principles, impedance control approaches were formally established a few years later, for example [2], providing a viable alternative to traditional position/force control architectures for physical interaction applications. The current state-of-the-art includes a wide range of impedance-based interaction control implementations, spanning machining applications, wearable robots, and transparency control in teleoperation [3]–[5].

Stiffness, damping, and inertia are the usual dynamic elements composing the desired impedance model. Stiffness and damping are the causally consistent choices based on the hypothesis that the environment is preferably described as an admittance [2]. The inertia can be the actual system inertia at the interaction port or a desired inertia when applying inertia shaping. Impedance assessment with graphical data usually highlights the spring-damper part of the model. Graphs plot the interaction force against the end-effector's deviation from its equilibrium point [6]–[8].

In impedance control, graphical representations such as ellipses and ellipsoids illustrate physical interactions. As described in [9], the *stiffness ellipse* represents the relationship between deviation and interaction forces in the task space. Each ellipse visually demonstrates the deviation-force relationship between Cartesian directions, such as x and y, when subjected to disturbance forces. The parameters of the diagonal of the Cartesian stiffness matrix define the theoretical ellipse axes, which serve as a reference for the realized task stiffness. This concept is also explored in [10], where the limitations of the realized stiffness are analyzed for the robot Jacobian and joint space limits, such as torque saturation. Although this approach has been applied to manipulators and legged robots in these studies, the complexity of three- or six-dimensional impedance formulations and hardware-related constraints prevent the consideration of damping and inertia parameters in this approach.

Graphical representations of stiffness are invaluable for adaptive and variable impedance controllers. In [11], the graphs showing the end-effector position and interaction force tracking are displayed separately over time to evaluate the desired impedance model on the adaptive reference controller. [12] apply a variable impedance control strategy with an integrated energy tank for passive interaction on industrial collaborative applications with incremental learning from demonstrations. Experimental data shows the end-effector deviation, interaction force, and equivalent stiffness during demonstrations. In contrast, [13] present a phase portrait with deviation versus the time derivative of the deviation ($e \times \dot{e}$) to demonstrate the stability of a variable impedance controller applied in a soft robot. The phase plane is the basis for qualitatively characterizing the stability of a dynamic system, identifying stable or unstable points and limit cycles in the state space.

The aforementioned studies use two-dimensional (2D) graphical representations to depict either the deviation-force curve or the deviation and force over time. Additionally, the three-dimensional (3D) graphs illustrate the stiffness ellipsoid, which is the realized stiffness across task space directions. Currently, there is no explicit relationship between impedance model parameters and their graphical representation for oscillatory input in one direction in either task or joint space. Furthermore, to our knowledge, no description encompasses

The associate editor coordinating the review of this manuscript and approving it for publication was Roberto S. Murphy (*Corresponding author: Cícero Zanette*).

This work was partially supported by São Paulo Research Foundation (FAPESP) under grants 2018/15472-9, 2021/03373-9, 2021/09244-6 and 2023/11407-6, and by Brazilian Federal Agency for Support and Evaluation of Graduate Education (CAPES) under grant 88887.817139/2023-00

L. F. D. Santos, Cícero Zanette, E. G. Vergamini, L. Maitan, and T. Boaventura are with the São Carlos School of Engineering, University of São Paulo, Brazil (e-mails: leonardo.felipe.santos@usp.br, cicero_zanette@usp.br, elisa.vergamini@usp.br, lucca.maitan@usp.br, and tboaventura@usp.br).

the phase plane, stiffness, and damping behavior simultaneously.

While previous definitions related to ellipses describe the relationship between task-space stiffness or damping in various directions, this work aims to describe impedance dynamics. We clarify the use of the term *ellipse* in impedance control to distinguish our concepts from previous definitions. A parametric representation is useful for descriptive stability and performance analysis. Additionally, it is essential to evaluate the impact of robot dynamics on the controller. This work addresses these issues with the following contributions:

- Introducing a novel 3D graphical representation of impedance, termed the *impedance space*, characterized by $e(t) \times \dot{e}(t) \times f_{int}(t)$. This representation extends traditional 2D plots: stiffness ($e(t) \times f_{int}(t)$), damping ($\dot{e}(t) \times f_{int}(t)$), and impedance phase space ($e(t) \times \dot{e}(t)$).
- Presenting a 3D elliptic curve in the *impedance space* for mass-spring-damper systems under sinusoidal input. The curve is developed from a 2D unity radius circle and undergoes linear transformations, parameterized by system mass, stiffness, and damping.
- Conducting experimental validation of the 3D elliptic curve by constructing the impedance space using real data and employing ellipse fitting for parametric analysis.

The focus of this paper is on active compliant control utilizing impedance analogy or similar control topologies specifically for torque-controlled robots. Furthermore, the proposed method has the potential to extend to other areas such as admittance control, physical interaction control, and various model-based methods. Table I aims to aid the reader on following the mathematical process of this paper.

This paper is structured as follows: Sec. II introduces relevant concepts, the impedance dynamic model, and presents 2D graphs for visualizing stiffness and damping with a sinusoidal input; Sec. III derives the parametric equation of the elliptic path in impedance space and explains the physical rationale behind this representation for evaluating impedance control; Sec. IV details the experimental setup and tests conducted to demonstrate the value of ellipse-based analysis; finally, Sec. V summarizes this work and suggests future research directions.

II. FUNDAMENTALS

In a classical perspective, a controller is characterized by its ability to track references and reject disturbances in time or frequency domain. This assessment applies to conventional robot control methods, e.g., force or position control. However, impedance control requires a different perspective. Relying on the physical design paradigm, impedance controllers shapes the interaction dynamics, employing physical reasoning rather than solely adhere to an input-output approach [14], [15].

That is, the goal is not to track a specific position or force but to control the *dynamic* relationship between a *generalized interaction force* $f_{int}(t)$ and the deviation $e(t)$ from an *equilibrium point* x_{eq} at a designated kinematic location, referred to as the *interaction port*. The equilibrium point can be interpreted simply as the controller reference.

TABLE I
VARIABLES AND THEIR MEANINGS

Variable	Meaning
t	Time
e	Position error
$\dot{e}$	Velocity error
f_{int}	Interaction force
Z	Impedance
Y	Admittance
k_d	Desired stiffness
d_d	Desired damping
m_d	Desired mass
a_i	Input amplitude
ω_i	Input angular frequency
$\boldsymbol{g}$	Tangent unit vector
$\boldsymbol{n}$	Normal unit vector
$\boldsymbol{b}$	Binormal unit vector
$\boldsymbol{T}$	Transformation matrix
$\boldsymbol{f}_1$, $\boldsymbol{f}_2$	Conjugate diameters
φ, ρ	3D rotation angles of $\boldsymbol{b}$
$\hat{\varphi}$, $\hat{\rho}$	Projected rotation angles of $\boldsymbol{b}$

A. Impedance vs Admittance Causality

The impedance and admittance causality are defined in terms of *effort* and *flow* [16]. Mechanically speaking, an impedance has velocity (flow) as input and force (effort) as output, virtually represented by a massless spring. In contrast, an admittance has force as input and velocity as an output, virtually represented by an infinitely rigid mass. In the Laplace domain and for a 1-DoF case, they can be defined as:

$$Z(s) = \frac{1}{Y(s)} = \frac{F_{int}(s)}{\dot{E}(s)} = \frac{F_{int}(s)}{sE(s)} \ , \tag{1}$$

where $Z(s)$ is the impedance, $F_{int}(s)$ the interaction force, and $E(s) = X_{eq}(s) - X(s)$ the position deviation , being $X_{eq}(s)$ the equilibrium position and $X(s)$ the current position.

As the physical interaction between two systems must be causal, i.e., one system must output what the other system expects as input, an impedance should always be coupled to an admittance, and vice-versa. When the robot interacts with rigid environments, which are preferably admittances, e.g. as shown on Fig. 1, the robot should behave as an impedance at the interaction port [2], [17].

B. System and deviation dynamics

For a mass-spring-damper designed impedance-controlled system, the impedance model is:

$$Z(s) = \frac{m_d\, s^2 + d_d\, s + k_d}{s} \ , \tag{2}$$

where m_d, d_d, and k_d are the desired mass, damping, and stiffness of the system, respectively. Under constrained movement, setting a periodic reference for the designated kinematic location gives the following deviation dynamics:

$$E(s) = \frac{a_i\, s}{s^2 + {\omega_i}^2} \ , \tag{3}$$

where a_i and ω_i are the amplitude and frequency of the deviation signal, respectively. Applying the Laplace inverse transform the time functions are obtained:

$$e(t) = \mathbf{L}^{-1}\{E(s)\} = a_i cos(t\omega_i) \ , \tag{4}$$

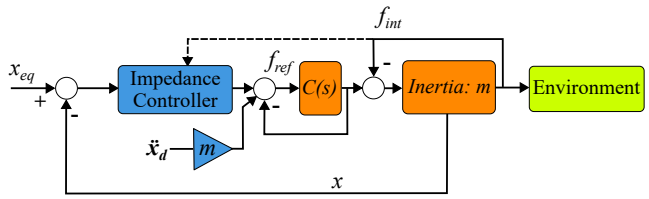

(a) Impedance control block diagram (1-DoF).

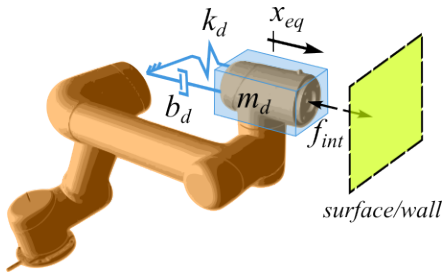

(b) Impedance control physical equivalence.

Fig. 1. In (a), the desired impedance parameters compose the impedance controller blocks in blue. The blocks in orange represent the robot's dynamics that physically interact with the environment (green). The inner torque/force controller $C(s)$ is usually tuned to track with high-fidelity the reference force f_{ref}. The interaction force feedback shown by a dashed line highlights its dependency on inertia shaping; In (b), a physical equivalence for an impedance controller acting at the end-effector of a manipulator robot.

$$f_{int}(t) = \mathbf{L}^{-1}\{Z(s)sE(s)\} = \\ = a_i \left(k_d cos(t\omega_i) - d_d\omega_i sin(t\omega_i) - m_d{\omega_i}^2 cos(t\omega_i)\right) \ . \quad (5)$$

Equations (4) and (5) describe the time-dependent components plot on $e(t) \times f_{int}(t)$ graphs for periodic input. And taking the time derivative of (4) one can see $\dot{e}(t) \times f_{int}(t)$ graph. Fig. 2 show these graphs. In the first case, the plot is in the stiffness plane, and if only stiffness is set in the impedance controller, the dynamics is linear and given by a line with slope equals to k_d; and, if any damping d_d is inserted in the controller, this line turns into an ellipse. The same applies to the second case, where the line slope is equal to d_d and it becomes an ellipse in case of adding a stiffness [18], [19].

Although these graphs are broadly adopted, no clarification of these 2D ellipses and the impedance model parameters was given before. As it will be clear here, these ellipses at the stiffness and the damping planes are 2D projections of a more complex 3D ellipse.

III. The Impedance Space

The *impedance space* is defined using an orthonormal basis. It encompasses three main aspects of impedance dynamics: the stiffness plane ($e \times f_{int}$), the damping plane ($\dot{e} \times f_{int}$), and the phase plane ($e \times \dot{e}$). It is defined as:

$$\boldsymbol{z}(t) = \begin{Bmatrix} e(t) \\ \dot{e}(t) \\ f_{int}(t) \end{Bmatrix} = e(t)\mathbf{i} + \dot{e}(t)\mathbf{j} + f_{int}(t)\mathbf{k} \ , \quad (6)$$

where $e(t)$ and $f_{int}(t)$ are position deviation and interaction force, respectively, and $\boldsymbol{i}$, $\boldsymbol{j}$, and $\boldsymbol{k}$ are the basis vectors. In the context of second-order autonomous (implicit time-dependent)

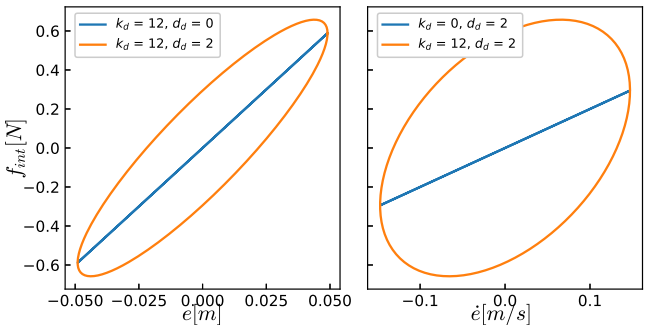

Fig. 2. Conventional 2D representation of the impedance stiffness and damping. Values of k_d in $\mathrm{N\,m^{-1}}$ and d_d in $\mathrm{N\,s\,m^{-1}}$. On the left side, on the $e(t) \times f_{int}(t)$ plane, plots for a pure spring, in blue, and a spring-damper, in orange. Note how the inclination of the main axis of the ellipse changes with respect to the line. On the right side, the reciprocal on the $\dot{e}(t) \times f_{int}(t)$ plane.

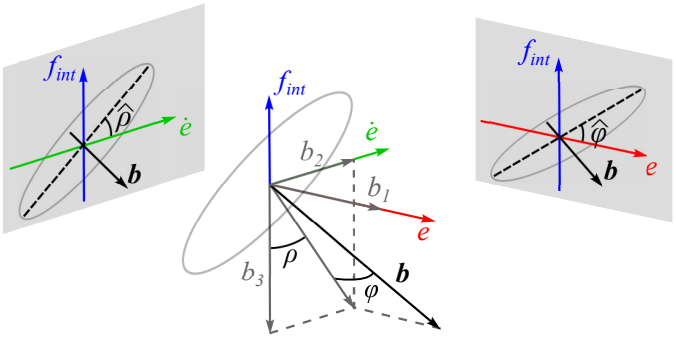

Fig. 3. The impedance ellipse binormal vector $\boldsymbol{b}$, normal to the trajectory plane of a mass-spring-damper impedance under sinusoidal input. The 3D elliptic trajectory is shown in light gray. The components of $\boldsymbol{b}$ are b_1 for the e-axis (red), b_2 for the $\dot{e}$-axis (green), and b_3 for the f_{int}-axis (blue). The left-hand side depicts the projection of the 3D graph on the damping plane, while the right-hand side shows the projection on the stiffness plane. Only in particular cases does the value of ρ, and φ matches the slope of the 2D ellipse major axis ($\hat{\rho}$, $\hat{\varphi}$) in these planes.

systems, represented by $\dot{\boldsymbol{x}} = f(\boldsymbol{x})$, the phase plane is the foundation for qualitative characterization of system stability through the phase portrait. Stable and unstable points, limit cycles, and multiple isolated equilibrium points are identified through the phase portrait [20], [21].

For a 2nd order dynamic system, as (2), under the periodic input (3), the time-dependent system trajectory in the impedance space lies in a plane. Consider the Frenet-Serret [22] triad: a unit vector $\boldsymbol{g}(t) = \dot{\boldsymbol{z}}(t)/\|\dot{\boldsymbol{z}}(t)\| \in \mathbb{R}^3$ tangent to the curve, a normal unit vector $\boldsymbol{n}(t) = \dot{\boldsymbol{t}}(t)/\|\dot{\boldsymbol{t}}(t)\| \in \mathbb{R}^3$ pointing to the center of the curve at $t > 0$, the binormal unit vector $\boldsymbol{b}(t)$, orthogonal to the trajectory, is:

$$\boldsymbol{b}(t) = \boldsymbol{g}(t) \times \boldsymbol{n}(t) = \begin{Bmatrix} \dot{e}(t) \\ \ddot{e}(t) \\ \dot{f}_{int}(t) \end{Bmatrix} \times \frac{d}{dt} \begin{Bmatrix} \dot{e}(t) \\ \ddot{e}(t) \\ \dot{f}_{int}(t) \end{Bmatrix} \ , \quad (7)$$

Using (4) and (5), vector $\boldsymbol{b}$ simplifies to:

$$\boldsymbol{b} = \begin{Bmatrix} b_1 \\ b_2 \\ b_3 \end{Bmatrix} = \frac{1}{\sqrt{\left(k_d - m_d\omega_i^2\right)^2 + d_d^2 + 1}} \begin{Bmatrix} k_d - m_d\omega_i^2 \\ d_d \\ -1 \end{Bmatrix} . \tag{8}$$

Through the orientation of $\boldsymbol{b}$ in the impedance space, Fig. 3, the sequential rotation angles φ and ρ are defined as follows:

$$\tan(\varphi) = -\frac{b_1}{\sqrt{b_2^2 + b_3^2}} = \frac{m_d\omega_i^2 - k_d}{\sqrt{d_d^2 + 1}} , \tag{9}$$

$$\tan(\rho) = -\frac{b_2}{b_3} = d_d , \tag{10}$$

where the negative sign in (10) and (9) is due to the right-handed coordinate systems convention.

As sequential rotation angles, φ and ρ have equivalent rotation matrices $\boldsymbol{T_e}(\rho), \boldsymbol{T_{\dot{e}}}(\varphi) \in \mathbb{R}^{3\times3}$. $\boldsymbol{T_e}(\rho)$ is a rotation around the e-axis. $\boldsymbol{T_{\dot{e}}}(\varphi)$ is a rotation around the $\dot{e}$-axis in the base rotated by $\boldsymbol{T_e}(\rho)$. Supposing that $z(t)$ can be parametrized by $\theta = \omega_i t, \in [0, 2\pi]$, and that in the impedance space the system is described by the following equation:

$$\boldsymbol{z}(\theta) = \boldsymbol{T_e}(\rho)\boldsymbol{T_{\dot{e}}}(\varphi)\boldsymbol{T_{f_{int}}} \begin{Bmatrix} \cos(\theta) \\ \sin(\theta) \\ 0 \end{Bmatrix} , \tag{11}$$

where $\boldsymbol{T_{f_{int}}}$ is defined as:

$$\boldsymbol{T_{f_{int}}} = \begin{bmatrix} & \boldsymbol{R} & & 0 \\ & & & 0 \\ 0 & 0 & & 1 \end{bmatrix} , \tag{12}$$

being $\boldsymbol{R} = \begin{bmatrix} \boldsymbol{f_1} & \boldsymbol{f_2} \end{bmatrix} \in \mathbb{R}^{2\times2}$ a matrix of the ellipse conjugate diameter $\boldsymbol{f_1}, \boldsymbol{f_2} \in \mathbb{R}^2$. Solving (11) for $\boldsymbol{T_{f_{int}}}$, the hypothesis are valid and defines:

$$\boldsymbol{R} = \begin{bmatrix} a_i\sqrt{\frac{(k_d - m_d\omega_i^2)^2}{d_d^2+1} + 1} & 0 \\ \frac{a_i d_d (k_d - m_d\omega_i^2)}{\sqrt{d_d^2+1}} & -a_i\omega_i\sqrt{d_d^2+1} \end{bmatrix} . \tag{13}$$

Then, it can be stated that the impedance model (2) under the input (3) describes a parametric 3D elliptic curve in the impedance space. This curve is described by a sequence of affine transformations upon the 2D parametric unit circle $[x\,,\,y] = [\cos(\theta)\,,\,\sin(\theta)]$, with $\theta \in [0, 2\pi]$ in the form of the Equation 11.

While the first two matrices are rotations, $\boldsymbol{T_{f_{int}}}$ scales and shears the parametric unit circle in the phase plane. Since the f_{int}-axis is normal to this plane, this transformation is named after it. With these matrices, the 3D elliptic curve can be derived without time dependence, being parameterized only by θ, the model constants and the input parameters ω_i and a_i.

Fig. 4 shows the isometric and perspective views of the impedance ellipse and its dependence on the impedance parameters k_d and d_d. The projection of the rotation angles ρ and φ into the $\dot{e} \times f_{int}$ and $e \times f_{int}$ planes is represented by $\hat{\rho}$ and $\hat{\varphi}$, respectively. The analytical expressions of these angle projections are very complex, highly nonlinear and dependent on all the desired impedance parameters[1]. Only in particular cases, the value of these projections simplify to $\hat{\rho} = \rho$, as depicted in Fig. 4c, and $\hat{\varphi} = \varphi$, in Fig. 4a.

This new approach elucidate the interpretation of the 2D ellipses, and the apparent slopes in the 2D projections. Figures 5 and 6 show how the slope changes according the sitffness and the damping, respectively. Moreover, the influence of the input frequency ω_i, is shown in Fig. 7. Even for the case $m_d = 0$ kg, where w_i affects only the $\boldsymbol{T_{f_{int}}}(2,2)$ term, the impedance ellipse changes significantly the shape.

IV. Experimental Impedance Ellipses

The experimental data was collected using a specially designed test bench named IC2D, shown in Fig. 8. The linear motor used in the experiment was the LinMot PS01-37x120F-HP-C (stator) and PL01-20x240 / 180HP (slider) models. The interaction force was measured using an Interface SMT1-250N load cell and and for the position we used the LM10IC001AB10F00 incremental encoder from RLS. A detailed description of the experimental bench is provided in [23], [24]. In both 2D and 3D, the impedance ellipse may also be plotted using experimental data to form the impedance state vector $z(t)$. The inner force controller, implemented in cascade with the impedance controller, was a PID with friction compensation through disturbance observer-based control (DOB) and load velocity compensation [25], [26]. Its tracking performance is shown in Fig. 9.

Nine experiments were conducted to demonstrate the parametric ellipses according to the parameters k_d and d_d. The interaction port was manually excited with a sinusoidal force. Despite the repeatability of the test bench, the accuracy of this parametric analysis was found to be sensitive to system force tracking fidelity and joint friction. A statistical treatment of the data is beyond the scope of this work. The experimental results support the present method qualitatively.

Fig. 10 shows the fitted ellipses for each parameter set, utilizing the stable direct least squares fitting algorithm from Halíř and Flusser [27]. Although the ellipse fit helps identify the rendered impedance, stiffness, and damping values, the performance of the inner-loop force tracking of the linear motor and the friction of the test bench affected the experimental data. Nevertheless, the ellipse fit captured the relevant graphical aspects in impedance space.

Using the impedance space allows new metrics to assess the rendered impedance against the desired one 3D ellipse. Examples include: 1) "interaction force fidelity" measures differences in force magnitudes for each specific point between ellipses; 2) "impedance 3D orientation error' compares the binormal vectors of ellipse planes, incorporating mass, damping, and stiffness; 3) "stiffness error" and "damping error" are specific metrics easily derived by comparing Equation 9 (for $m_d = 0$) and Equation 10, respectively, which are angles defined in the 3D space, rather than relying on their 2D projections.

Moreover, in [28] was present a stiffness plot, where the data presented a so called *hysteresis*-like shape which is attributed to the damping only. However, as it is clear now, this shape correlation with damping is described by an ellipse projection, not a hysteresis phenomenon which is related to friction forces.

[1]Full expressions at https://github.com/leggedrobotics-usp/impedance_control_benchmark

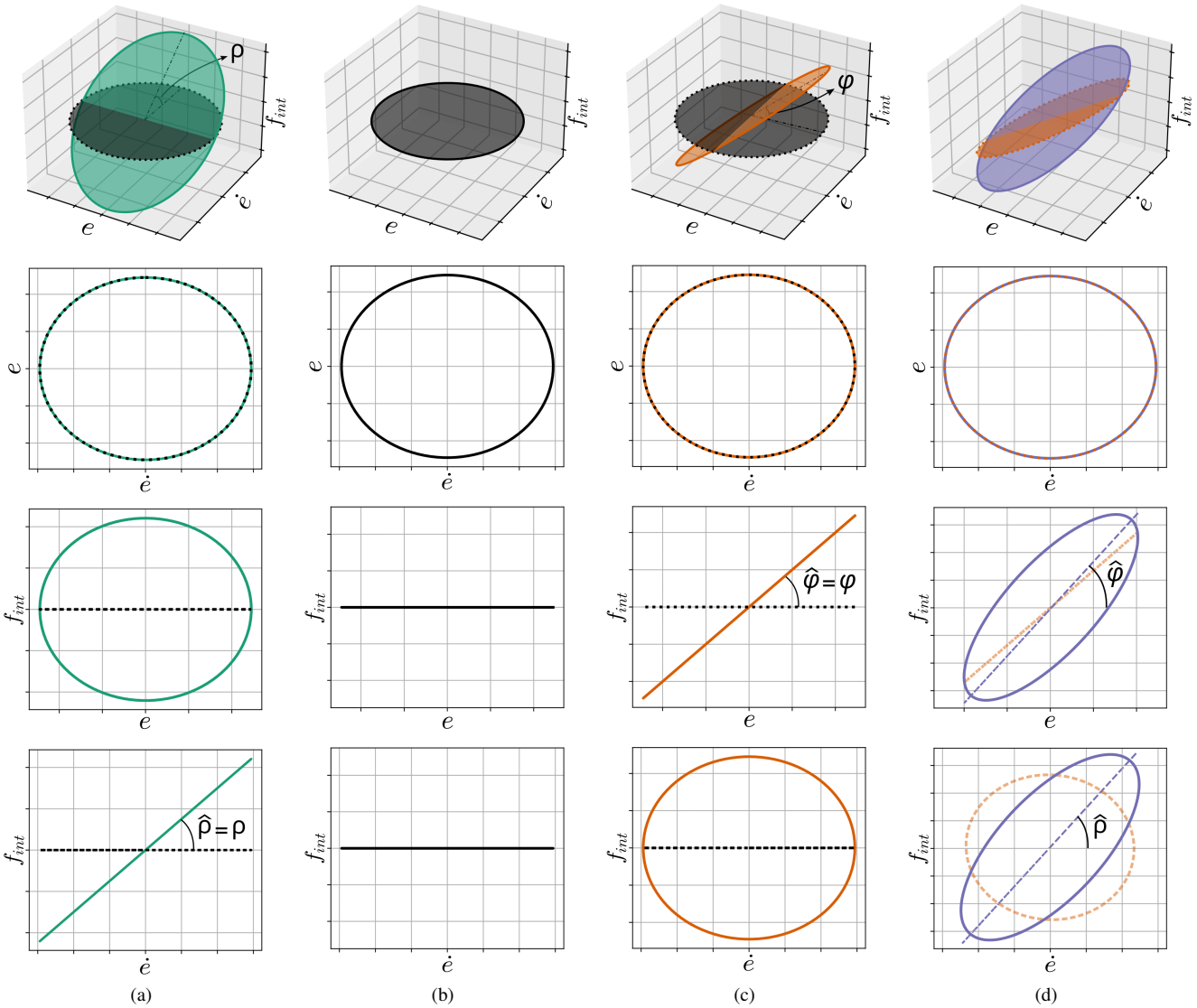

Fig. 4. Visualization of the 3D theoretical impedance plots and its projections. Each column represents a specific combination of impedance parameters k_d and d_d ($m_d = 0$ for all of them), while the rows show different projection of the 3D impedance plot for each case. The first row, in particular, shows the 3D *impedance space*. In (b), where $k_d = 0$ and $d_d = 0$, only the original unit circle is plotted, from which the other columns derive. In (a), $d_d \neq 0$ is added, and the original circle, in black, is elongated and then rotated by ρ around the e axis. An ellipse appears in the 3D plot, with a projection on the plane $\dot{e} \times f_{int}$ being a straight line with the slope given by $tan(\hat{\rho}) = tan(\rho) = d_d$. In (c), $k_d \neq 0$ is added to the original circle in (b), which is elongated and then rotated by φ around the $\dot{e}$ axis in this case. The 2D ellipse projection on $e \times f_{int}$ is also a straight line, with a slope given by $tan(\hat{\varphi}) = tan(\varphi) = k_d$. Last but not least, in (d), the original circle is transformed into a 3D ellipse with $k_d \neq 0$ and $d_d \neq 0$. In this case, the 2D projections in both $e \times f_{int}$ and $\dot{e} \times f_{int}$ planes are also ellipses. It is important to highlight that, for these 2D projected ellipses, $tan(\hat{\varphi}) \neq k_d$ and $tan(\hat{\rho}) \neq d_d$. In particular, in the $e \times f_{int}$ plane it is possible to see how the inclination changes with respect to the pure stiffness case of (c).

V. Conclusions & Outlook

This paper introduced and discussed a novel representation of mechanical impedance ellipses in a 3D impedance space $e(t) \times \dot{e}(t) \times f_{int}(t)$. A 3D parametric elliptical curve describes the impedance dynamics using linear transformations, which are functions not only of the impedance controller parameters m_d, k_d, and d_d, but also of the input amplitude a_i and frequency ω_i. This modeling and representation approach fosters parameter-oriented analysis of experimental time series using the designed dynamic behavior as a reference. The impedance rendering performance obtained with experimental data in this paper was limited by the inner force controller's tracking capabilities and the amplitude and frequency input fluctuations within each cycle due to the manual excitation. These factors also affect systems with a higher number of degrees of freedom. For n-DoF systems, one challenge is associating joint-level force tracking with the robot Jacobian and the impedance space trajectory for a given direction in task space. As a final remark, this paper highlights that the phase space $e(t) \times \dot{e}(t)$, included in the presented impedance space, supports further nonlinear and energy-based analysis. Future developments include calculating the mentioned met-

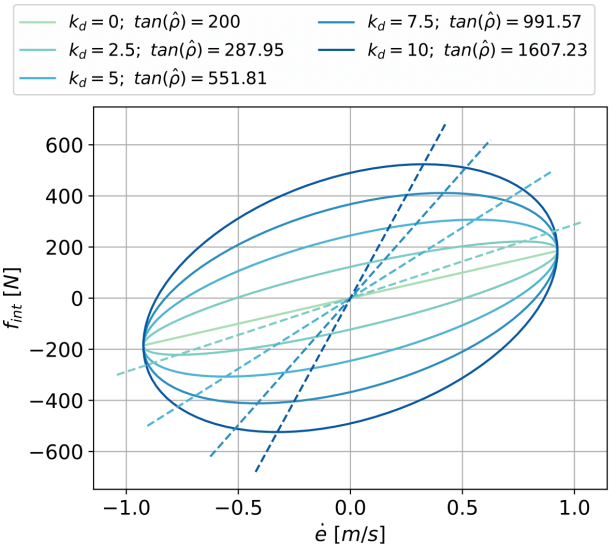

Fig. 5. Plot of the 2D projected ellipse in the $\dot{e} \times f_{int}$ plane, with a fixed $d_d = 200\ \mathrm{N\,s\,m^{-1}}$. Values of k_d in $\mathrm{N\,m^{-1}}$. When a stiffness k_d is added to the impedance controller, the slope of the ellipse major axis $tan(\hat{\rho})$ may significantly differ from d_d.

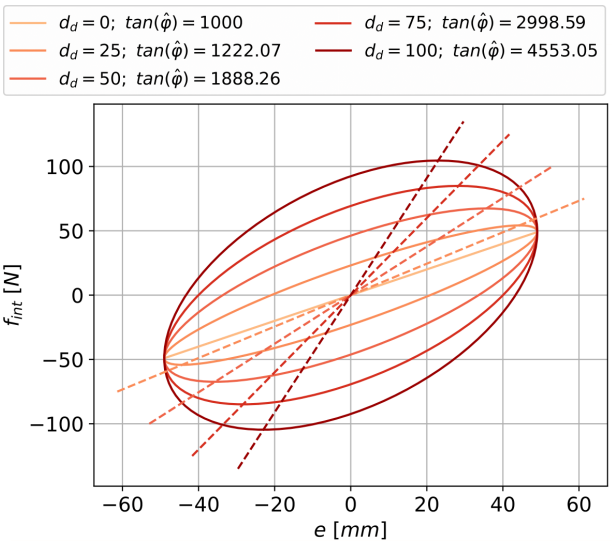

Fig. 6. Plot of the 2D projected ellipse in the $e \times f_{int}$ plane, with a fixed $k_d = 1000\ \mathrm{N\,m^{-1}}$. Values of d_d in $\mathrm{N\,s\,m^{-1}}$. When a damping d_d is added to the impedance controller, the slope of the ellipse major axis $tan(\hat{\varphi})$ may significantly differ from k_d.

rics, extending the analysis including the impedance state $\ddot{e}(t)$ and the influence of inertia shaping.

ACKNOWLEDGMENTS

The authors would like to thank the Legged Robotics Group of the Robotics Laboratory of the São Carlos School of Engineering, University of São Paulo.

REFERENCES

[1] S. Grillner, "The role of muscle stiffness in meeting the changing postural and locomotor requirements for force development by the ankle extensors," *Acta Physiologica Scandinavica*, vol. 86, no. 1, pp. 92–108, 1972, DOI: 10.1111/j.1748-1716.1972.tb00227.x.

[2] N. Hogan, "Impedance control: An approach to manipulation: Part I — Theory," *Journal of Dynamic Systems, Measurement, and Control*, vol. 107, no. 1, pp. 1–7, 1985.

[3] Y. Huo, X. Li, X. Zhang, X. Li, and D. Sun, "Adaptive intention-driven variable impedance control for wearable robots with compliant actuators," *IEEE Transactions on Control Systems Technology*, vol. 31, no. 3, pp. 1308–1323, 2022, DOI: 10.1109/TCST.2022.3222728.

[4] M. Panzirsch, H. Singh, X. Xu, A. Dietrich, T. Hulin, E. Steinbach, and A. Albu-Schaeffer, "Enhancing the force transparency of the energy-reflection-based time-domain passivity approach," *IEEE Transactions on Control Systems Technology*, 2024, DOI: 10.1109/TCST.2024.3458831.

[5] S. Lloyd, R. A. Irani, and M. Ahmadi, "Improved accuracy and contact stability in robotic contouring with simultaneous registration and machining," *IEEE Transactions on Control Systems Technology*, 2024, DOI: 10.1109/TCST.2023.3348749.

[6] T. Boaventura, J. Buchli, C. Semini, and D. G. Caldwell, "Model-based hydraulic impedance control for dynamic robots," *IEEE Transactions on Robotics*, vol. 31, no. 6, pp. 1324–1336, 2015, DOI: 10.1109/TRO.2015.2482061.

[7] P. Song, Y. Yu, and X. Zhang, "A tutorial survey and comparison of impedance control on robotic manipulation," *Robotica*, vol. 37, no. 5, pp. 801–836, 2019, DOI: 10.1017/S0263574718001339.

[8] S. Yoo, W. Lee, and W. K. Chung, "Impedance control of hydraulic actuation systems with inherent backdrivability," *IEEE/ASME Transactions on Mechatronics*, vol. 24, no. 5, pp. 1921–1930, 2019, DOI: 10.1109/TMECH.2019.2932132.

[9] M. Focchi, T. Boaventura, C. Semini, M. Frigerio, J. Buchli, and D. G. Caldwell, "Torque-control based compliant actuation of a quadruped robot," in *2012 12th IEEE international workshop on advanced motion control (AMC)*. IEEE, 2012, pp. 1–6, DOI: 10.1109/AMC.2012.6197133.

[10] A. Ajoudani, N. G. Tsagarakis, and A. Bicchi, "On the role of robot configuration in cartesian stiffness control," in *2015 IEEE international conference on robotics and automation (ICRA)*. IEEE, 2015, pp. 1010–1016, DOI: 10.1109/ICRA.2015.7139300.

[11] J. Zhang, H. Li, Q. Liu, and S. Li, "The model reference adaptive impedance control for underwater manipulator compliant operation," *Transactions of the Institute of Measurement and Control*, vol. 45, no. 11, pp. 2135–2148, 2023.

[12] M. Dalle Vedove, E. Lamon, D. Fontanelli, L. Palopoli, and M. Saveriano, "A passivity-based variable impedance controller for incremental learning of periodic interactive tasks," in *2024 IEEE 20th International Conference on Automation Science and Engineering (CASE)*. IEEE, 2024, pp. 2604–2609.

[13] M. Mazare, S. Tolu, and M. Taghizadeh, "Adaptive variable impedance control for a modular soft robot manipulator in configuration space," *Meccanica*, vol. 57, no. 1, pp. 1–15, 2022.

[14] A. Sharon, N. Hogan, and D. E. Hardt, "Controller design in the physical domain," *Journal of the Franklin Institute*, vol. 328, no. 5-6, pp. 697–721, 1991, DOI: 10.1016/0016-0032(91)90049-9.

[15] J. Lachner, F. Allmendinger, S. Stramigioli, and N. Hogan, "Shaping impedances to comply with constrained task dynamics," *IEEE Transactions on Robotics*, vol. 38, no. 5, pp. 2750–2767, 2022, DOI: 10.1109/TRO.2022.3153949.

[16] N. Hogan, "Modularity and causality in physical system modeling," *Journal of dynamic systems, measurement, and control*, vol. 109, no. 4, pp. 384–391, 1987, DOI: 10.1115/1.3143871.

[17] P. J. Gawthrop and G. P. Bevan, "Bond-graph modeling," *IEEE Control Systems Magazine*, vol. 27, no. 2, pp. 24–45, 2007, DOI: 10.1109/MCS.2007.338279.

[18] S. K. Charles and N. Hogan, "Stiffness, not inertial coupling, determines path curvature of wrist motions," *Journal of neurophysiology*, vol. 107, no. 4, pp. 1230–1240, 2012, DOI: 10.1152/jn.00428.2011.

[19] Z. Ranko, Ángel Valera Fernández, and P. J. G. Gil, "Impact and force control with switching between mechanical impedance parameters," *IFAC Proceedings Volumes*, vol. 38, no. 1, pp. 169–174, 2005, DOI: 10.3182/20050703-6-CZ-1902.01298.

[20] H. Khalil, *Nonlinear Systems*, ser. Pearson Education. Prentice Hall, 2002, ISBN: 9780130673893.

[21] F. Verhulst, *Nonlinear Differential Equations and Dynamical Systems*, ser. Universitext. Springer Berlin Heidelberg, 2006, ISBN: 9783540609346.

[22] J. Stewart, "Vector functions: arc lenth and curvature," in *Calculus: Early Transcendentals*, 6th ed. Belmont, CA: Thomson Brooks/Cole, 2008, pp. 830–838, ISBN: 9780495382737.

[23] E. G. Vergamini, L. Felipe dos Santos, C. L. A. Zanette, Y. Moreno, F. M. Escalante Ortega, and T. Boaventura, "Construction of an

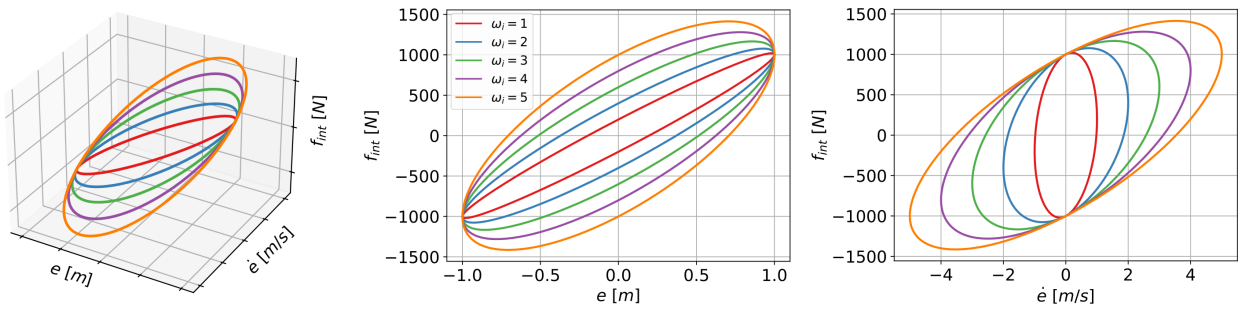

Fig. 7. Influence of the input frequency ω_i, in $\mathrm{rad\,s^{-1}}$, on the impedance ellipses for the parameters $m_d = 0$ kg, $k_d = 1000\ \mathrm{N\,m^{-1}}$ and $d_d = 200\ \mathrm{N\,s\,m^{-1}}$.

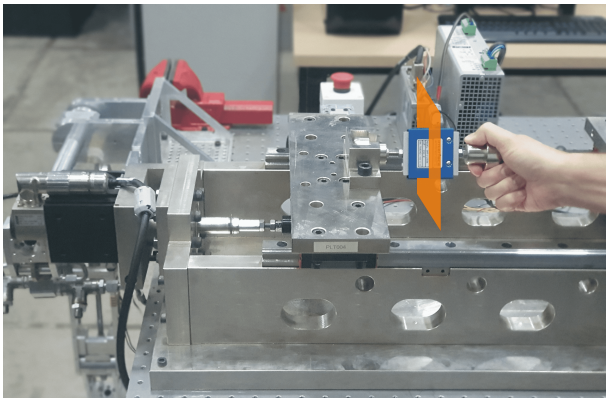

Fig. 8. Experimental setup. The interaction port is highlighted in orange. The interaction force was provided by a human hand, and a linear encoder measured the position. From left to right: linear motor, platform, load cell. The encoder is behind the platform, measuring its position.

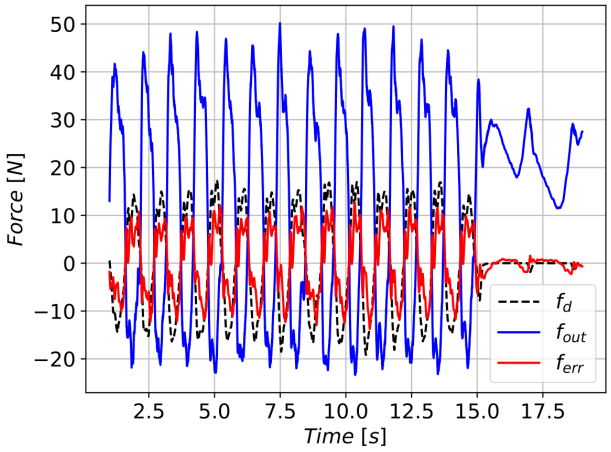

Fig. 9. Experimental data showing the reference tracking of the inner force controller for the experiment with $k_d = 0\ \mathrm{N\,m^{-1}}$ and $d_d = 200\ \mathrm{N\,s\,m^{-1}}$. The plot shows the desired interaction force (f_d, black), the force error ($f_{err} = f_{int} - f_d$, red), and the controller output (f_{out}, blue). The controller output is expressed in Newtons and corresponds to the force command; this value is later converted into motor current using the actuator's force-to-current constant. This force tracking performance influences the rendered impedance.

impedance control test bench," in *Proceedings of the 27th International Congress of Mechanical Engineering*, ser. COB2023. ABCM, 2023, DOI: 10.26678/abcm.cobem2023.cob2023-0847. [Online]. Available: https://www.researchgate.net/publication/378419899

[24] E. Vergamini, L. F. Santos, and C. Zanette, "Ic2d project," https://github.com/leggedrobotics-usp/ic2d, 2023.

[25] E. Dimo and A. Calanca, "Environment aware friction observer with applications to force control benchmarking," *Actuators*, vol. 13, no. 2, 2024, DOI: 10.3390/act13020053. [Online]. Available: https://www.mdpi.com/2076-0825/13/2/53

[26] T. Boaventura, M. Focchi, M. Frigerio, J. Buchli, C. Semini, G. A. Medrano-Cerda, and D. G. Caldwell, "On the role of load motion compensation in high-performance force control," in *2012 IEEE/RSJ International Conference on Intelligent Robots and Systems*, 2012, pp. 4066–4071, DOI: 10.1109/IROS.2012.6385953.

[27] R. Halır and J. Flusser, "Numerically stable direct least squares fitting of ellipses," in *Proc. 6th International Conference in Central Europe on Computer Graphics and Visualization. WSCG*, vol. 98. Citeseer, 1998, pp. 125–132, ISSN: 1213-6972. [Online]. Available: https://api.semanticscholar.org/CorpusID:15772208

[28] C. Ott, *Cartesian Impedance Control of Redundant and Flexible-Joint Robots*, ser. Springer Tracts in Advanced Robotics. Springer, 2008, ISBN: 9783540692553.

Leonardo F. dos Santos holds a degree in Mechatronics Engineering from the São Carlos School of Engineering at the University of São Paulo (2021). His interests lie in robotics, systems modeling and control, both in academia and industry. Leonardo is currently a member of the Legged Robotics Group and is pursuing is PhD within the FAPESP Young Researcher Project entitled 'Impedance control of hydraulic actuators for robots with legs and arms'. He is also a member of SENAI CIMATEC's robotics division, where he contributes to initiatives focusing on robotic manipulation for underwater inspection, maintenance, and repair.

Cícero Zanette received his B.Sc degree in Mechanical Engineering from the Federal University of São Carlos, Brazil, in 2021. During his undergraduate studies, he worked with computational simulations in the area of induced cracks in high-hardness ceramics during laser-assisted machining processes utilizing FEM. He received his M.Sc degree in Dynamics and Mechatronics from the São Carlos School of Engineering of the University of São Paulo, Brazil, where he worked with the Legged Robotics Group in the development of metrics for comparison of hybrid impedance and admittance controllers. He is currently pursuing his D.Sc. degree in the same research group.

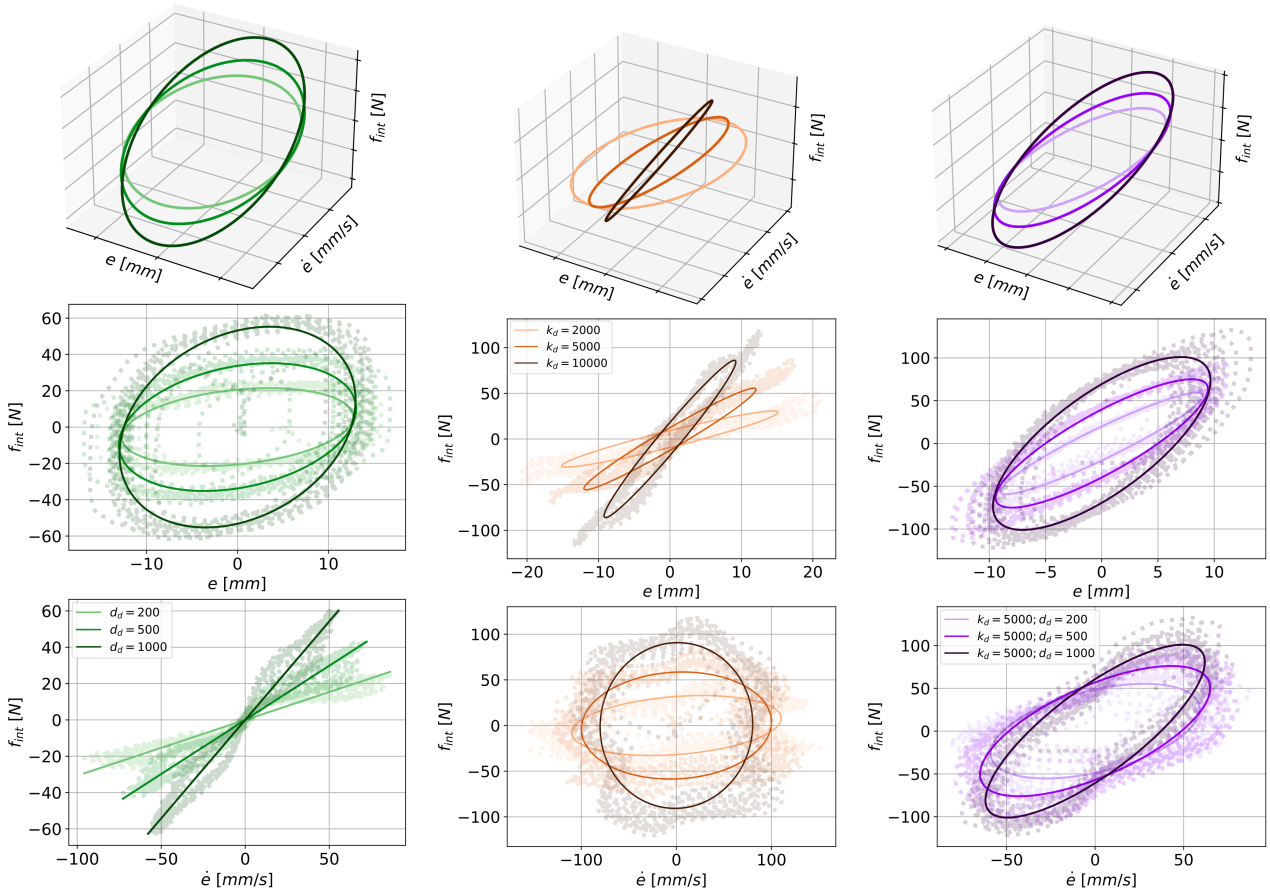

(a) (b) (c)

Fig. 10. Experimental results, all with $m_d = 0$ kg. (a) for $k_d = 0\ \mathrm{N\,m^{-1}}$ and varying the value of d_d one can see that in the $\dot{e} \times f_{int}$ plane the straight line slope increases with d_d and in the $e \times f_{int}$ plane the ellipse widens due to the projection as expected; (b) for $d_d = 0\ \mathrm{N\,s\,m^{-1}}$ and varying the value of k_d, one can see that in the $e \times f_{int}$ plane, the slope of the ellipse major axis increases with k_d and in the $\dot{e} \times f_{int}$ plane the ellipse widens due to the projection as expected. The widening of the ellipse in the $e \times f_{int}$ plane is due to unwanted damping, mostly caused by the test bench itself. As can be seen, the openings are practically the same, as the damping of the bench does not change; (c) for both parameters k_d and d_d varying, the effects combine on both planes.

Elisa G. Vergamini graduated in Mechanical Engineering from the Federal University of São Carlos, Brazil, in 2020. In 2018, Elisa studied for a year at the École Nationale Supérieure de Techniques Avancées, in the undergraduate course in Mechanical Engineering with an emphasis on Intelligent Systems. In 2022, she carried out a research internship abroad for six months (BEPE - FAPESP) at the Altair Robotics Lab at the University of Verona. In 2024, Elisa completed her master's degree at the Robotics Laboratory of the Department of Mechanical Engineering of the São Carlos School of Engineering of the University of São Paulo, at the Legged Robots Group. She is currently pursuing her PhD in the same Research Group.

Lucca Maitan holds a degree in Mechatronics Engineering from the University of São Paulo (2021). He has experience in the areas of Robotics, Mechatronics, Automation, and software development. During his undergraduate studies, he worked on scientific initiation projects and his final thesis at the Robotic Rehabilitation Laboratory of the Department of Mechanical Engineering at EESC - USP, focusing on exoskeleton control. Since the second semester of 2023, he has been pursuing a Master's degree in the legged robots laboratory at EESC - USP, specializing in control of electric and hydraulic actuators and impedance control for robotic legs.

Thiago Boaventura received his B.Sc. and M.Sc. degrees in Mechatronics Engineering from the Federal University of Santa Catarina, Brazil, in 2009. He received his Ph.D. degree in Robotics from a partnership between the Italian Institute of Technology and the University of Genoa in Italy in 2013. Then, he joined as a post-doctoral researcher at the Agile Dexterous Robotics Lab at ETH Zurich in Switzerland. There, he was mainly involved in the EU FP7 BALANCE project with a focus on the collaborative impedance control of exoskeleton robots. Thiago is an Assistant Professor at the São Carlos School of Engineering of the University of São Paulo. He is the founder and director of the Legged Robotics Group, a branch of the Robotics Laboratory. He has a strong background in model-based force and impedance control, as well as in hydraulic actuation.